DOI: 10.61782/fa.2025.0406

FORUM ACUSTICUM
EURONOISE 2025

FLOW CHARACTERISATION USING PIV TO OPTIMISE MICROPHONE WINDSCREENS FOR ON-BOARD SELF-NOISE MEASUREMENTS OF A MULTICOPTER (UAV) UNDER DIFFERENT FLIGHT CONDITIONS

Julian Benz[1*] **Christoph Heigl**[1] **Felix Czwielong**[1]
Andreas Gründer[2] **Jörg Franke**[2] **Stefan Becker**[1]
[1] Institute of Fluid Mechanics,
Friedrich-Alexander-University Erlangen-Nuremberg, 91058 Erlangen, Germany
[2] Institute for Factory Automation and Production Systems,
Friedrich-Alexander-University Erlangen-Nuremberg, 91058 Erlangen, Germany

ABSTRACT

Accurately measuring the self-noise of unmanned aerial vehicles (UAVs) is crucial for acoustic characterisation, noise reduction optimisation, and gaining public acceptance and certification of these aircraft. An on-board measurement setup allows direct and flexible detection of acoustic phenomena in different flight conditions, without the need for external sensor installations with the problem of continuously changing measurement distance and a complex measurement setup. For reliable measurements, especially at higher flight or wind speeds, an effective microphone windscreen is essential. This windscreen should ideally shield the microphone from ambient and propeller airflow while introducing minimal additional turbulence noise, which could otherwise mask the UAV's self-noise and reduce measurement accuracy. In this study, the airflow around the microphone of a quadrocopter UAV was experimentally analysed for different flight conditions using stereo PIV measurements and a wind tunnel. Based on the results, optimisation possibilities for the microphone windscreen solution were investigated in an aeroacoustic wind tunnel. Starting from commercially available windscreens, different designs were investigated and refined to effectively suppress hydrodynamic pressure fluctuations that overlap with the UAV self-noise. The results illustrate how airflow patterns change in different flight situations and highlight practical optimisation strategies to improve the accuracy of UAV self-noise measurements.

Keywords: *multicopter, PIV, noise, microphone, windscreen*

**Corresponding author: julian.benz@fau.de.*

1. INTRODUCTION

Multirotors, commonly known as drones or Unmanned Aerial Vehicles (UAVs), have evolved rapidly from futuristic concepts to practical tools used in diverse commercial and public service applications. Examples of their widespread adoption include autonomous package deliveries already operational in regions such as Australia [1] and upcoming implementations planned in the United Kingdom and elsewhere [2]. Additionally, their inherent flexibility has enabled them to perform various specialized tasks, ranging from media production, such as aerial photography and videography, to medical logistics like the rapid transport of blood samples [3], and critical roles in rescue and reconnaissance missions [4–6] or in the agriculture [7]. The increased use of UAVs introduces significant challenges, most notably the issue of noise emissions [8]. Drone-related noise pollution has become a contentious issue, often leading to public concern and regulatory scrutiny. Engineers and developers thus face the dual challenge of effectively reducing noise emissions while si-

multaneously adhering to regulatory acoustic limits, similar to those established for other technical equipment like heat pumps [9]. Moreover, enhancing energy efficiency remains crucial, as it directly affects the operational range and flight duration of multirotor systems. Prior research at the Chair of Fluid Mechanics (LSTM) has investigated correlations between propeller-generated thrust and noise emissions under controlled hover conditions, confirming a strong link between aerodynamic performance and acoustic output [10]. However, to thoroughly characterize and understand UAV acoustics, it is essential to expand analyses beyond hover conditions. Realistic flight operations, including horizontal, climbing, and descending maneuvers, involve complex aerodynamic interactions that significantly influence the acoustic footprint of the aircraft. The reason for this is that each of these flight maneuvers exhibits specific aerodynamic characteristics [11] and phenomena also known from helicopters. These include the vortex ring state in vertical flight, blade-vortex interactions, flow separations, or Mach number effects [12]. In order to capture the noise emissions of multirotors, there are essentially two approaches: external measurements using microphone(s) on the ground or direct onboard measurements with microphone(s) on the drone itself. However, external measurements are associated with drawbacks, as they usually require a multitude of specifically arranged microphones [13], entail complex evaluations, and the variability of the drone's position during flight as well as atmospheric sound propagation effects [14] limit the measurement accuracy. An on-board measurement using one or more microphones offers a flexible and practical alternative, allowing acoustic data to be recorded directly and continuously during flight. Nevertheless, other challenges arise, particularly due to hydrodynamic pressure fluctuations caused by the propeller flow as well as the self-motion of the multirotor and ambient wind. Previous studies have shown that, especially at higher flight speeds, significant masking effects due to hydrodynamics impair the measurement of the actual self-noise [10]. Furthermore, it has been demonstrated that the positioning of the microphone has a significant impact on the measured sound spectrum. While other publications have positioned microphones on lateral arms [15], future placement is intended to be centrally above the drone, near the horizontal center of mass and without altering the moments of inertia about the horizontal axes. This positioning reduces unwanted influences on flight stability and agility, enables better comparability of the measurements. Furthermore, as demonstrated in the volumetric PIV investigation by Wolf [16], is that in the suction area, where significantly less turbulence occurs compared to a placement beneath the drone. This study clearly illustrated not only the reduction in turbulence but also the behavior of the flow—including blade vortices and other flow phenomena during various flight maneuvers—in different regions around the drone. For our purposes, it is particularly important to analyze how the flow behaves in the suction area, especially in terms of flow direction and turbulence levels, where the effects of the drone's body flow are most pronounced. Therefore, the subsequent analysis will focus on characterizing the flow in this critical region.

2. FLOW CHARACTERIZATION

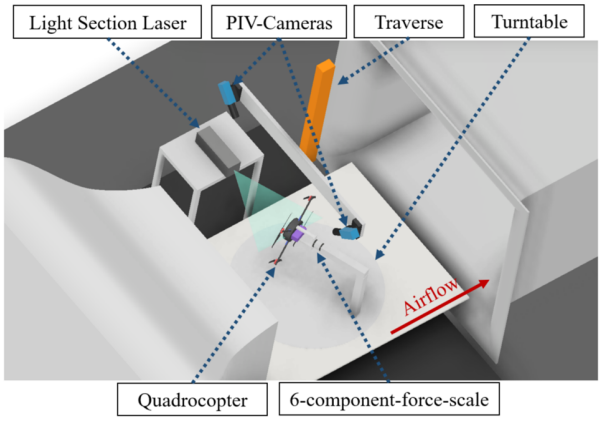

Figure 1. The measurement setup.

To enable future investigations of wind protection variants under realistic conditions, a detailed flow analysis using Stereo-PIV is conducted. The measurements were carried out in the wind tunnel of the Chair of Fluid Mechanics (LSTM). This wind tunnel has a cross-sectional area of $B = 1.87\,\mathrm{m} \times H = 1.40\,\mathrm{m}$ and a test section length of $L = 2.4\,\mathrm{m}$, featuring a central test table and an integrated turntable. A schematic picture of the measurement setup is shown in Fig. 1.

The quadrocopter used for the measurements was equipped with $D = 15$-inch propellers (T-Motor NS15x5) and has a flight weight without payload of $m_{\mathrm{Quadrocopter}} = 3.1\,\mathrm{kg}$. This UAV represents a typical 5-kg class system with a payload capacity of 2 kg, providing an excellent research platform. As shown in Fig. 2, the quadrocopter has canopy with an oval planform and proper extrusion to facilitate a better characterization of its surrounding airflow. Most of the onboard electronics, are housed within

the canopy and the battery hangs under it, so there is a minimal influence to the flow above, with only the electronic speed controlers slightly outside the canopy.

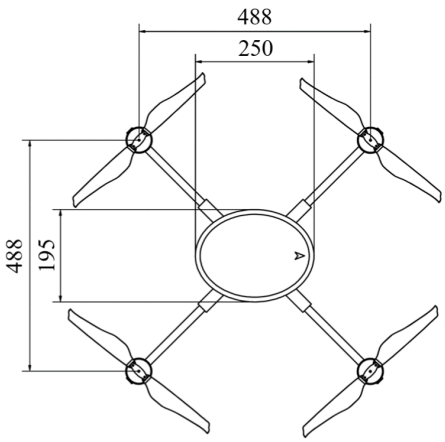

Figure 2. Dimensions of the investigated quadrocopter.

For the Stereo-PIV measurements, two *PCO.2000* cameras with *Sigma* lenses (f = 18–35 mm F1.8) and Scheimpflug adapters were employed. The system was calibrated and aligned using a specialized calibration device and an optical calibration plate. Scheimpflug optics ensured that both cameras shared the same focal plane, allowing reliable three-dimensional (XYZ) measurements. Particular care was taken to ensure that the seeding particles (propylene glycol) were accurately assigned throughout the measurement volume. The flow was illuminated by a pulsed Nd:YAG laser (*Quantel Twins BSL 200*), and data evaluation was performed using the software *PIVView3C*. The measured plane was located centrally between the rotors of the multirotor, as illustrated in Fig. 3. This plane is particularly relevant for understanding the flow, as the measurement microphone will be positioned here in the future.

The current and rotational speed were individually set and monitored for each motor. The multirotor was mounted on a 6-component force balance for the simultaneous measurement of aerodynamic forces on the turntable. The propeller thrust for each flight condition was validated using the 6-component force balance. The relative deviation between the experimentally measured thrust F_{meas} and the theoretically required thrust for weight compensation at a tilt angle θ was calculated as:

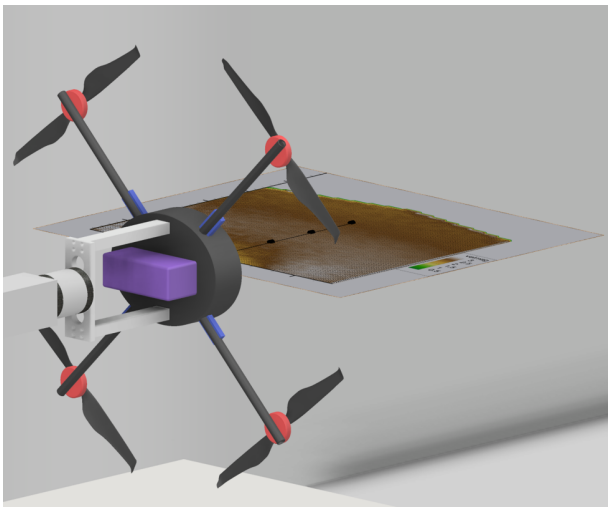

Figure 3. Illustration of the investigated measurement plane.

$$\Delta F_{\%} = \left(\frac{F_{\text{meas}} \cos(\theta)}{m\, g} - 1 \right) \times 100\,\%. \qquad (1)$$

The rotor speeds were determined experimentally during several test flights, with each relevant flight maneuver being performed multiple times and the recorded rotational speeds and currents averaged. These averaged rotor speeds were then precisely reproduced for each motor seperately in the wind tunnel.

2.1 Hover Case

In a hover case no external airflow is applied, which poses a challenge for PIV measurements since, without additional flow, the seeding particles are not sufficiently transported to characterize the velocity field. To overcome this, the airflow generated by the propellers was utilized. The thrust produced by the rotating propellers induces a passive airflow in our closed-loop wind tunnel (Göttinger design), that transports the particles. However, this passive flow leads to a circulation that establishes a relative airflow of approximately $v_{passive} = 1.86\,\text{m/s}$. This passive flow reduces the inflow angle on the propeller blades and consequently diminishes the generated thrust, so that the expected $T = 30.5$ N for hover is not fully reached, as seen in Fig. 4. To compensate, the propeller speed was increased by 200 rpm, which in turn raised the passive airflow to about $v_{passive} = 1.94\,\text{m/s}$. As a result, instead of a pure hover, the condition is more akin to a slow climb

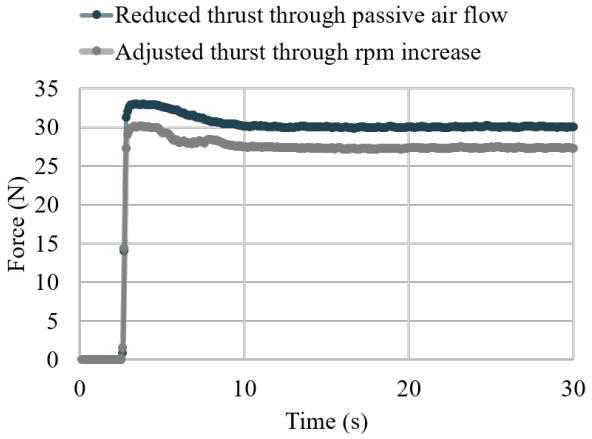

Figure 4. Thrust curve in hover case through passive air flow after turning on the motors at 2 s.

at $v_{vertical} = 1.94\,\mathrm{m/s}$. Analysis of the flow field in Fig. 5 shows that at a distance of the Z-coordinate in the body-fixed frame, $Z_{UAV} = 100\,\mathrm{mm}$ from the drone a stagnation zone with low velocities between $1\,\mathrm{m/s} \leq u \leq 1{,}5\,\mathrm{m/s}$ exists; at $Z_{UAV} = 200\,\mathrm{mm}$ and $Z_{UAV} = 300\,\mathrm{mm}$ the velocity increases to $v \approx 2.5\,\mathrm{m/s}$, and then decreases again to about $v = 2\,\mathrm{m/s}$ at $Z_{UAV} = 400\,\mathrm{mm}$. Furthermore, the flow direction remains largely consistent with only minor deflections very close to the drone at $Z_{UAV} \approx 50\,\mathrm{mm}$, where slight redirection components are observed.

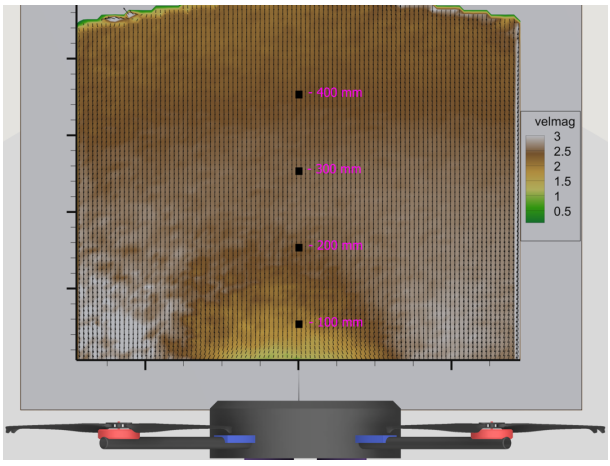

Figure 5. Averaged flow field at $v_{horizontal} = 5\,\mathrm{m/s}$ with the Z-coordinate indicated in the body-fixed frame.

2.2 Horizontal Flight with a Speed of 5 m/s

The conditions for the case of $v_{\text{horizontal}} = 5\,\mathrm{m/s}$ are summarized in Table 1.

Parameter	$v_{\text{horizontal}} = 5\,m/s$
Tilt Angle, θ [°]	4.1
Thrust Deviation, $\Delta F\%$	1.08%

Table 1. Flight conditions at $v_{\text{horizontal}} = 5\,m/s$.

Figure 6 illustrates the averaged flow field obtained under these conditions. The analysis reveals a pronounced stagnation zone in the immediate vicinity of the multirotor body, where the local flow velocity drops to approximately $v = 3.5\,\mathrm{m/s}$. At a distance of around $Z_{UAV} = 100\,\mathrm{mm}$ from the vehicle, distinct velocity peaks emerge, reaching up to $v = 8\,\mathrm{m/s}$. As the distance from the multirotor increases further, the flow velocity gradually diminishes, converging to the nominal flight speed of $v_{\text{horizontal}} = 5\,\mathrm{m/s}$. Moreover, while the flow direction near the body exhibits significant deviations, it increasingly aligns with the flight trajectory at larger distances.

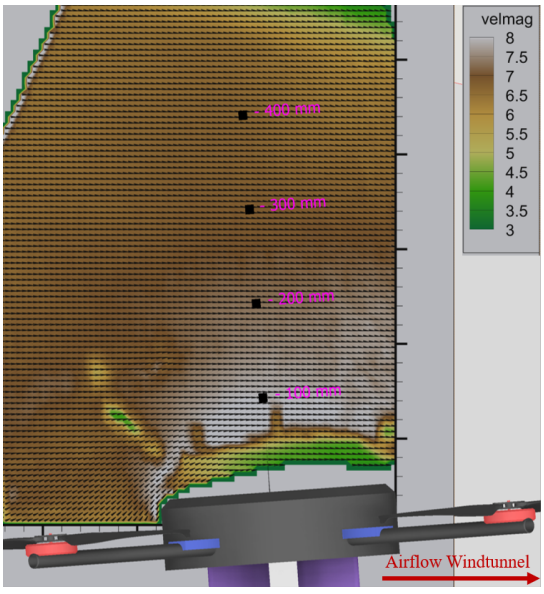

Figure 6. Averaged flow field at $v_{\text{horizontal}} = 5\,\mathrm{m/s}$ with the Z-coordinate indicated in the body-fixed frame.

2.3 Horizontal flight with a speed of 10 m/s

The conditions for the case of $v_{\text{horizontal}} = 10\,\text{m/s}$ are summarized in Table 2.

Parameter	$v_{\text{horizontal}} = 10\,m/s$
Tilt Angle, θ [°]	10.0
Thrust Deviation, $\Delta F\%$	2.98%

Table 2. Conditions at $v_{\text{horizontal}} = 10\,m/s$.

A similar flow pattern is observed at a higher horizontal flight speed of $v_{horizontal} = 10\,\text{m/s}$, as shown in Fig. 7. Here is also a strong stagnation zone was observed immediately at the multirotor body, which, at a distance of $Z_{UAV} = 100$ mm, exhibits strong flow velocity peaks of up to $v = 12\,\text{m/s}$. This increased velocity then continuously decreases with further distance and approaches the actual flight speed. Again, it is evident that near the multirotor body there are significant deviations in the flow direction from the actual flight direction, while at greater distances the flow direction corresponds to the flight trajectory.

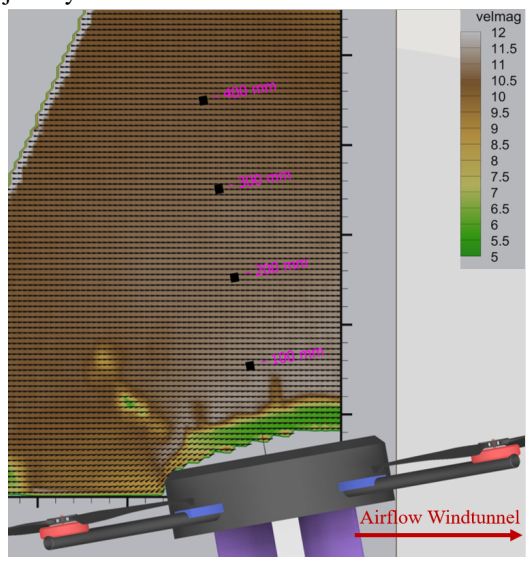

Figure 7. Averaged flow field at $v_{horizontal} = 10\,\text{m/s}$ with the Z-coordinate indicated in the body-fixed frame.

2.4 Horizontal Flight with a Speed of 15 m/s

For the case of $v_{\text{horizontal}} = 15\,\text{m/s}$ the conditions are shown in Table 3.

Parameter	$v_{\text{horizontal}} = 15\,m/s$
Tilt Angle, θ [°]	16.6
Thrust Deviation, $\Delta F\%$	-2.98%

Table 3. Flight conditions for $v_{\text{horizontal}} = 15\,m/s$.

In the $v_{horizontal}$ = 15 m/s case (see Fig. 8), a similar behavior is observed as in the previously investigated horizontal flow fields at different speeds. Very close to the drone, within less than $Z_{UAV} = 100$ mm, a stagnation zone with considerably reduced flow velocities $v \approx 8$ m/s is present, accompanied by strong flow deflections near the drone body. At a distance of around $Z_{UAV} = 100$ mm, a pronounced velocity peak is observed, reaching $v \approx 15$ m/s. With increasing distance from the drone, the flow velocity gradually decreases and eventually converges to the nominal flight speed of $v_{horizontal}$ = 15 m/s at about $Z_{UAV} = 400$ mm. Moreover, the flow direction progressively aligns with the flight trajectory of the drone.

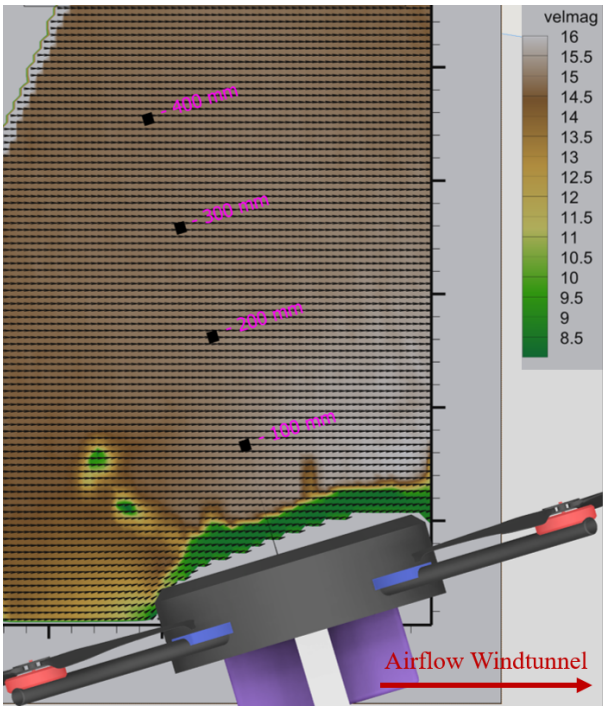

Figure 8. Averaged flow field at $v_{horizontal} = 15\,\text{m/s}$ with the Z-coordinate indicated in the body-fixed frame.

2.5 Summary of Flow Conditions

The present measurements reveal that in all investigated flight maneuvers, a pronounced stagnation zone develops in close proximity to the drone body. At approximately $Z_{UAV} = 80\,\text{mm}$ from the drone, the flow field exhibits significantly increased velocities, with local speeds exceeding the nominal flight speed of up to 60%. As the distance from the drone increases, the flow gradually aligns with the flight trajectory and approaches the vehicle's actual speed. At $Z_{UAV} = 200\,\text{mm}$, the velocities remain slightly elevated compared to the flight speed, while from around $Z_{UAV} = 300\,\text{mm}$ onward, the measured flow velocity essentially matches the nominal flight speed. Although a larger separation, such as $Z_{UAV} = 400\,\text{mm}$, would provide even more favorable flow conditions, it would necessitate a considerably larger mounting structure for the microphone.

These findings are critical for the future design of the wind protection system. The windscreen should be strategically positioned to avoid the stagnation zone, where elevated flow velocities are very close to and the directions the flow are changing. It is also expected that there is higher turbulence intensity within the stagnation region. So it is advisable to place the microphone in an area where the flow has already aligned with the flight trajectory and speed. Future investigations will focus on a detailed analysis of the turbulence distribution and its impact on the measurements, ultimately guiding the optimal positioning of the wind protection.

3. INVESTIGATION OF VARIOUS WIND PROTECTION VARIANTS

In future investigations, the characterized flow conditions will serve as the basis for evaluating various wind protection variants under realistic conditions. To illustrate the potential of these designs, preliminary results from experiments conducted in an aeroacoustic wind tunnel are presented in Fig. 9. These measurements were performed at an approach velocity of $v = 10\,\text{m/s}$ with a 90° incidence angle (i.e., perpendicular to the microphone). The following wind protection variants were tested:

- *MTG* Standard Foam Wind Protection 50 mm (referred to in the spectrum as *Foam*)
- *Rycote Baseball* (referred to in the spectrum as *Baseball*)
- *Rycote Cage with foam + Deadcat* (referred to in the spectrum as *Deadcat*)
- *Rycote Classic Softie* (referred to in the spectrum as *RCS*)
- *Rycote Super Softie* (referred to in the spectrum as *RSS*)

Figure 9 provides a comparison of the different wind protection variants at $v = 10\,\text{m/s}$. Additionally, two microphones were placed outside the primary flow region, and their averaged measurements (denoted as 'outside' in the spectrum) were used as reference values to account for the baseline hydrodynamic influence. The external measurements consistently showed low flow-induced noise, whereas significant differences became apparent when evaluating the wind protection variants.

Notably, the standard foam wind protection (*Foam*) exhibited average sound pressure levels of approximately $L_{p,\text{Mittel}} \approx 48\,\text{dB}$, similar to those observed for the *RSS* and *Baseball* variants. In contrast, the *Deadcat* demonstrated a considerable advantage over the foam by reducing overall sound pressure levels by roughly $\Delta L_{p,\text{Mittel}} \approx 4\,\text{dB}$. This improvement is particularly pronounced in the low-frequency range ($f < 500\,\text{Hz}$), where hydrodynamic pressure fluctuations are most influential. The *Deadcat* achieves a sound level reduction of about $\Delta L_p \approx 11\,\text{dB}$ compared to the foam there. Moreover, the frequency responses of the variants differ significantly in certain ranges. For instance, a switching behavior is observed where the *Foam* variant outperforms *RSS* in specific frequency bands, and vice versa. In some cases, characteristic spectral peaks, presumably due to flowinduced effects or structural noise from the wind protectors, were also detected and warrant further investigation.

At a higher approach velocity of $v = 20\,\text{m/s}$, even more pronounced differences emerge (see Fig. 10). Under these conditions, the classic foam variant performs the poorest. Although its performance up to about $f > 100$ Hz remains comparable to that of the other variants, from around $f < 200$ Hz onward its sound pressure levels increase dramatically by at least 10 dB compared to all other wind protection types a trend that continues well into the high kHz range. Of course it is not made for such flow velocities, it is more like a reference in this case. In contrast, the *RCS* variant performs best in the low-frequency range $f < 300$ Hz but exhibits a significant level increase at higher frequencies. Overall, when the entire frequency spectrum is considered, the *Deadcat* consistently shows

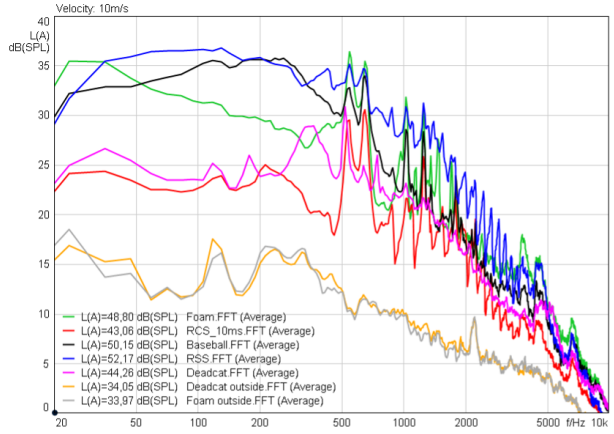

Figure 9. Comparison of the different wind protection variants at a flow velocity of $v = 10\,\mathrm{m/s}$.

the best performance, achieving an overall improvement of $\Delta L_p \approx 17\,\mathrm{dB}$ compared to the classic foam. The presence of characteristic peaks in some of the spectra suggests specific flow-induced components or inherent structural noise from the wind protectors, aspects that will be examined in more detail in future studies.

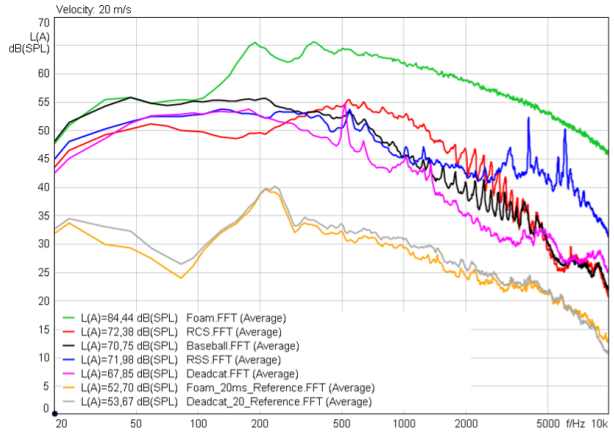

Figure 10. Comparison of the different wind protection variants at a flow velocity of $v = 20\,\mathrm{m/s}$.

Lastly, it is important to note the varying sizes of the wind protection variants. In drone applications, where size and weight are critical parameters, finding an optimal balance between effective wind protection and minimal impact on the vehicle is essential. Future work will focus on refining this balance under realistic flow conditions.

4. CONCLUSION AND OUTLOOK

By employing Stereo-PIV measurements in a wind tunnel, we characterized the complex airflow around a quadrocopter under various flight conditions. Our analysis revealed that, regardless of the maneuver, a pronounced stagnation zone develops in close proximity to the drone body, with local velocities exceeding the nominal flight speed of up to 60%. As the distance increases, the flow gradually aligns with the flight trajectory and converges to the actual movement speed, highlighting the importance of sensor placement for accurate noise measurements. Furthermore, we evaluated several wind protection variants in the aeroacoustic wind tunnel. Preliminary results indicate that commercially available windscreens, particularly the *Deadcat* variant, can significantly reduce the impact of hydrodynamic pressure fluctuations on the measured sound pressure levels. Notable differences in the frequency response among the tested variants emphasize the need for an optimized design that minimizes additional turbulence and noise while maintaining a compact form factor. Looking ahead, future work will focus on a more comprehensive analysis of the turbulence distribution within the stagnation zone and its impact on acoustic measurements. This will enable further refinement of the wind protection design, ensuring optimal microphone placement. The goal is to develop a universally applicable windscreen that reliably isolates the UAV's self-noise, thereby improving measurement accuracy and facilitating broader acceptance of UAV operations in both commercial and regulatory contexts.

5. REFERENCES

[1] E. Visontay, E. V. Transport, and u. a. reporter, "'We don't stop for red lights': drone deliveries take off as Australian regulators prepare for air traffic boom," *The Guardian*, Aug. 2024.

[2] BBC, "Amazon picks Darlington for drone deliveries trial," *BBC News*, Jan. 2025.

[3] S. W. R. Aktuell, "Klingt nach Science Fiction, ist aber wahr: Hier werden Blutproben bald per Drohne verschickt," *SWR Aktuell*, Mar. 2025.

[4] Z. Fang and A. V. Savkin, "Strategies for Optimized UAV Surveillance in Various Tasks and Scenarios: A Review," *Drones*, vol. 8, p. 193, May 2024.

[5] M. Erdelj, E. Natalizio, K. R. Chowdhury, and I. F. Akyildiz, "Help from the Sky: Leveraging UAVs for

Disaster Management," *IEEE Pervasive Computing*, vol. 16, pp. 24–32, Jan. 2017.

[6] W. Schmidbauer, C. Jänig, E. Vits, T. Gruebl, S. Sauer, N. Weller, K. Kehe, F. Holzapfel, T. Lüth, K. G. Kanz, E. Rittinghaus, and P. Biberthaler, "Ein neues Rettungskonzept für Schwerstverletzte in militärischen und zivilen Großschadenslagen: DRONEVAC," *Notfall + Rettungsmedizin*, Aug. 2023.

[7] R. Guebsi, S. Mami, and K. Chokmani, "Drones in Precision Agriculture: A Comprehensive Review of Applications, Technologies, and Challenges," *Drones*, vol. 8, p. 686, Nov. 2024.

[8] E. Thalheimer, "Community Acceptance of Drone Noise," *INTER-NOISE and NOISE-CON Congress and Conference Proceedings*, vol. 263, pp. 913–924, Aug. 2021.

[9] BMDV, "BMDV - Lärmvorsorge und Lärmsanierung an Bundesfernstraßen," Dec. 2018.

[10] J. Benz, A. Gründer, F. Czwielong, and S. Becker, "Acoustic Self-Noise Measurement of a Quadcopter (UAV) in Flight with Focus on Data Acquisition, Microphone Position, and Microphone Wind Protection," 2024. Artwork Size: 1336090 Bytes Pages: 1336090 Bytes.

[11] Y. Yang, Y. Liu, Y. Li, E. Arcondoulis, and Y. Wang, "Aerodynamic and Aeroacoustic Performance of an Isolated Multicopter Rotor During Forward Flight," *AIAA Journal*, vol. 58, pp. 1171–1181, Mar. 2020.

[12] B. G. Wall, *Grundlagen der Hubschrauber-Aerodynamik*. Berlin, Heidelberg: Springer Berlin Heidelberg, 2015.

[13] A. Nash and J. Kennedy, "In Flight Evaluation of UAV Noise Emission,"

[14] A. Ziemann and K. Balogh, "Gekoppelter Atmosphäre-Boden-Einfluss auf die Schallausbrei- tung einer höher gelegenen Schallquelle," 2006.

[15] J. Meister and R. Pieren, "UAV noise emission characterisation using a compact on-board measurement system,"

[16] C. C. Wolf, D. Schanz, C. Schwarz, A. Heintz, J. Bosbach, T. Strübing, and A. Schröder, "Volumetric wake investigation of a free-flying quadcopter using Shake-The-Box Lagrangian particle tracking," *Experiments in Fluids*, vol. 65, p. 152, Oct. 2024.